# Small High-Resolution Angular Displacement Measurement Technology Based on Near-Field Image Acquisition

Xingdan Jia, Qiuhua Wan, Hai Yu, Ying Sun, and Changhai Zhao, *Member, IEEE*

***Abstract*— Advances in fine photoelectric displacement measurement technology have made image angular displacement measurement technology via imaging method a popular research topic; it is now easier than ever to realize small-scale high-resolution angular displacement measurement. This paper proposes a small-sized high-resolution image angular displacement measurement technique based on near-field image acquisition. A measuring mechanism based on the lensless near-field image acquisition is first established. Next, based on the error code problem, a space-value-based code value correction algorithm is proposed. Finally, the proposed device is validated on an experimental system. The proposed technology can achieve 21-bit resolution and 20.14" angle measurement accuracy. The results presented here may provide a workable foundation for further research on image-type fine photoelectric displacement measurement technology.**

***Index Terms*— Subdivision, high precision, high resolution, angular displacement measurement, image detector.**

## I. Introduction

FINE photoelectric displacement measurement technology is an integration of light, machine, and electricity. As the heart of digital measurement and control instruments, it has been widely used in servo control and aerospace measurement practices [1], [2]. Traditional photoelectric angular displacement measurement technology contains a photoelectric conversion element which converts an optical signal into an electrical signal, then secures a current absolute angle value through the phase information of the Moiré fringe signal. Photoelectric angular displacement measurement technology with grating as the core has been developed alongside metrology grating technology.

Traditional photoelectric angular displacement measurement technology is very sophisticated [3]–[5]. The incremental and absolute hybrid angular displacement measuring device designed by Heidenhain of Germany for the Italian Galileo telescope control system, for example, has an angular resolution of 0.01" and an accuracy of 0.036". It is the most accurate angular displacement measuring device available today. The scale density of the grating, however, restricts the resolution of the traditional device. The conventional angular displacement measuring device does not readily achieve high resolution and high precision angular displacement measurement if it is small in size.

Requirements for the volume, weight, accuracy, resolution, and reliability of the angular displacement measurement devices are growing increasingly stringent as technologies continually advance. The conventional angular displacement measuring device must be equipped with a relatively large grating for sufficiently precise high-resolution angular displacement measurement, which makes the measuring device altogether large in size.

VLSI technology has markedly improved the resolution, sensitivity, stability, and other technical indicators of image detectors. Advancements in digital imaging technique and image processing technology [6]–[10] have yielded a new type of photoelectric converter, the image detector, which is widely used in the field of fine photoelectric displacement measurement. The image detector allows for fine photoelectric displacement measurement and can be used to measure angular displacement with high precision and high resolution even on a small-sized measuring device.

There have been many contributions to the image-based angular displacement measurement field in recent years. NASA took the lead in researching high-precision image-based angular displacement measuring devices with a resolution of 0.01" [11], [12]; researchers at the Changchun Institute of Optics and Mechanics recently used lens magnification imaging to achieve 21-bit resolution and 6.33" angular displacement measurement accuracy [13]. Research institutions in Serbia [14], Japan [15], [16], Spain [17], [18], South Korea [19], China [20] and Argentina [21] have also achieved notable results. Most extant techniques are based on pixel-level angular displacement measurement, where optical lens magnifying imaging is usually used to improve the grating image quality and the device is large in volume. Indeed, small-sized and high-resolution angular displacement measurement is not yet fully possible.

The remainder of this paper is organized as follows. Section II presents the measurement mechanism of image

Manuscript received March 3, 2019; accepted April 6, 2019. Date of publication April 15, 2019; date of current version July 3, 2019. This work was supported in part by the National Natural Science Foundation of China under Grant 51605465 and in part by the Science and Technology Development Program of Jilin Province under Grant 20180520184JH. The associate editor coordinating the review of this paper and approving it for publication was Dr. Ioannis Raptis. *(Corresponding author: Qiuhua Wan.)*

X. Jia is with the Changchun Institute of Optics, Fine Mechanics, and Physics, Chinese Academy of Sciences, Changchun 130033, China, and also with the University of Chinese Academy of Sciences, Beijing 100049, China (e-mail: jiaxingdan@126.com).

Q. Wan, H. Yu, Y. Sun, and C. Zhao are with the Changchun Institute of Optics, Fine Mechanics, and Physics, Chinese Academy of Sciences, Changchun 130033, China (e-mail: wanqh@ciomp.ac.cn).

Digital Object Identifier 10.1109/JSEN.2019.2911095

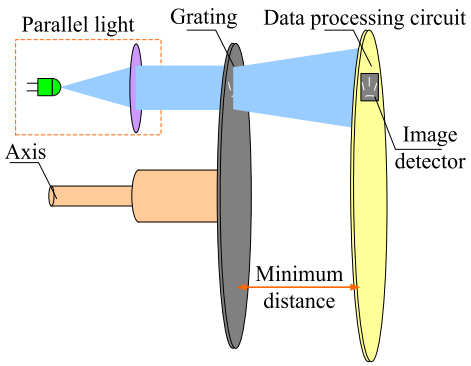


Fig. 1. Image angular displacement measurement.

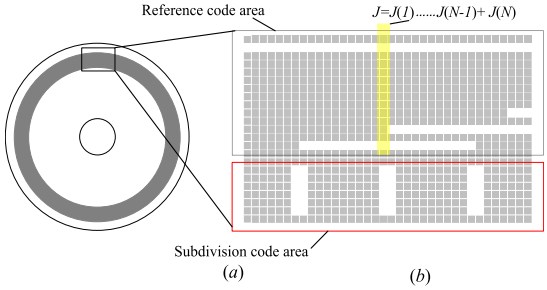


Fig. 2. Grating pattern. (a) Grating. (b) Part of grating unfolding drawing.

angular displacement measurement technology, the grating image decoding method, and a sub-pixel angular displacement subdivision algorithm. Section III presents a space-value-based code value correction algorithm. Section IV discusses our measurement device prototype and presents our test results. Section V provides a brief summary and conclusion.

## II. Image-Type Angular Displacement Measurement Technology Mechanism

Image-based angular displacement measurement technology uses image detectors instead of traditional photoelectric conversion elements to replace Moiré-striped photoelectric signals with pixel gray value information. A schematic diagram of this measurement technique is shown in Fig. 1. The setup includes a main shaft, a parallel light source, a grating, an image detector, and a data processing circuit. Its working principle is as follows: the parallel light source is irradiated onto the image detector through the grating and the reticle on the grating is projected onto the image detector, then the data processing circuit decodes the reticle information in the image collected by the image detector and performs subdivision calculation to obtain the current high-resolution absolute angle information.

The light source markedly affects the device's measuring performance. The lighting mode also affects its resolution. In our setup, we used transmissive illumination to place the grating between the parallel light source and the image detector; this helps to secure a clear grating image and reduce the complexity of angular displacement measurement.

When parallel light passes through the grating reticles, a diffraction phenomenon is generated which significantly affects the grating image quality. Light diffraction can be alleviated when the grating is close to the image detector. A shorter light-source wavelength results in less diffraction and thus better imaging effects in the grating. In this study, we used the lens-free near-field image acquisition method to bring the image detector close to the grating without affecting its rotation. As discussed below, this effectively reduces the volume of the image angular displacement measuring device.

### A. Circular Grating Decoding Principle

Grating reticle design is a very important step in establishing an image angular displacement measurement device. Different reticle forms and widths have significant influence on the accuracy and resolution of the device. Several circles of reference reticles representing the reference code are scribed in the circumference of the grating; they have higher bits when they are closer to the center of the grating. For the purposes of angular displacement subdivision, subdivided reticles are scribed between two adjacent reference codes of the outermost circle of the grating code disc. The grating pattern is shown in Fig. 2.

The image detector acquires an image of the grating which then must be decoded. The image detector output contains both position and pixel value information with a one-to-one correspondence between the two. To decode the circular grating, we divided the grating image into a reference code (*R.code*) identification area and a subdivision code (*S.code*) identification area as shown in Fig. 2(b).

The distribution of pixel values at the center line of the image detector is $J = \{z_0, z_1, z_2, z_3 \ldots\ldots z_m\}$ in *R.code* identification area, $z_m$ is a pixel value, and $m$ is the number of pixels at the center line of the image detector. When the grating scribes the $N$-circle reference reticle, the image detector center line is divided into $N$ segments in the *R.code* identification area so that each segment contains one reference reticle and each segment contains $M$ pixels.

$$M = \text{int}\left(\frac{m}{N}\right) \tag{1}$$

When the distribution of pixel values of the $i$-th segment is $J(i) = \{z_0(i), z_1(i), z_2(i), z_3(i)\ldots\ldots z_M(i)\}$, then the pixel mean in the $i$-th $(1 \le i \le N)$ segment can be expressed as follows:

$$\overline{z} = \frac{1}{M} \times \sum_{j=0}^{M} z_j\,(i), \quad (1 \le i \le N) \tag{2}$$

The relationship between the pixel mean $\overline{z}$ and threshold $Y_R$ is determined, then the information $\alpha(i)$ represented by the $i$-th reference mark is determined as follows:

- When $\overline{z} \ge Y_R$, then $\alpha(i) =$ "1";
- When $\overline{z} < Y_R$, then $\alpha(i) =$ "0".

The code values represented by the $N$ reference reticles are obtained by the mean value of each segment for the $N$ segments as calculated by Formula (2). The *R-code* of the $N$-bit is then determined according to the grating coding mode. The $n$- bit *S.code* is determined by the distribution of the reticles on both sides of the image detector center line. After decoding and subdivision, the device can achieve

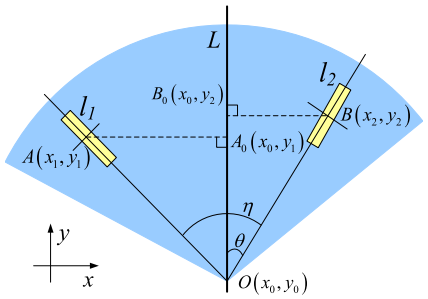


Fig. 3. Subdivision algorithm.

$(N + n)$-bit angular displacement measurement. The current absolute angular position can be expressed as:

$$\varphi = R.code \times 2^n + S.code \tag{3}$$

### *B. Sub-Pixel Angular Displacement Subdivision Algorithm*

The minimum reference symbol now needs to be subdivided to achieve higher-resolution angular displacement measurement. The subdivision angle is calculated between the subdivided reticles on both sides of the image detector center line as per the *S.code* value. A schematic diagram of the subdivision algorithm is shown in Fig. 3.

The coordinate system is also shown in Fig. 3, where $O$ is the center of the grating, $L$ is the center line of the image detector, $l_1$ and $l_2$ are the subdivided reticles on both sides of the image detector center line $L$, and $A$ and $B$ are the centroids of the subdivided reticles $l_1$ and $l_2$. $A_0$ and $B_0$ are projection points of the centroids $A$ and $B$ on the image detector center line $L$, respectively. $\eta$ is the angle between the subdivided reticles $l_1$ and $l_2$, that is, the angle between the gratings; $\theta$ is the subdivided angle value.

We next set the threshold $Y_s$. In *S.code* identification area, when the pixel value of a certain point is larger than $Y_s$, the point is considered to be within the subdivided reticle. The region $\{\Omega\}$ of the subdivided reticle is determined by the set of all the pixel points with pixel values larger than $Y_s$. The following centroid algorithm is used to calculate the centroids $A$ and $B$ of the subdivision reticle:

$$\begin{cases} U = \dfrac{\sum\limits_{x,y\in\Omega} x \times p(x,y)}{\sum\limits_{x,y\in\Omega} p(x,y)} \\ V = \dfrac{\sum\limits_{x,y\in\Omega} y \times p(x,y)}{\sum\limits_{x,y\in\Omega} p(x,y)} \end{cases} \tag{4}$$

where $\{\Omega\}$ is the region where the subdivision line is located, $x$ is the abscissa of the pixel in the region $\{\Omega\}$, $y$ is the ordinate of the pixel in the region $\{\Omega\}$, and $p(x, y)$ is pixel value at the position $(x, y)$. The positions of the centroids $A$ and $B$ are calculated as $A(x_1, y_1)$ and $B(x_2, y_2)$, respectively, where $U = \{x_1, x_2\}$, $V = \{y_1, y_2\}$. The image detector center line $L$ is located at $x = x_0$, so $AA_0 = x_0\text{-}x_1$, $BB_0 = x_2\text{-}x_0$.

In $\Delta AOA_0$ and $\Delta BOB_0$, according to the sine theorem:

$$\frac{\sin\theta}{\sin(\eta-\theta)} = \frac{\frac{BB_0}{BO}}{\frac{AA_0}{AO}} \tag{5}$$

and because the subdivided reticles are evenly distributed in the radial direction, $AO = BO$ (Fig. 3). Since $\theta$ is between $(0,\eta)$, $\eta$-$\theta$ is also between $(0,\eta)$. $\eta\left(\eta = \frac{360°}{2^N}\right)$ is small, and for convenience of calculation, $\sin(\theta) \approx \theta$, $\sin(\eta-\theta) \approx \eta-\theta$ can be approximated. Equation (5) can be rewritten as:

$$\frac{\theta}{\eta-\theta} = \frac{BB_0}{AA_0} \tag{6}$$

Formula (6) can be obtained by finishing

$$\theta = \frac{BB_0}{AA_0 + BB_0} \times \eta \tag{7}$$

and substituting the values of $AA_0$ and $BB_0$ into Eq. (7) yields:

$$\theta = \frac{(x_2 - x_0)}{(x_0 - x_1) + (x_2 - x_0)} \times \eta = \frac{x_2 - x_0}{x_2 - x_1} \times \eta \tag{8}$$

which provides the subdivision angle value between $l_1$ and $l_2$ for sub-pixel level angular displacement subdivision. The calculated angular displacement subdivided value is normalized and mapped to $2^n$ for the sake of intuitive observation. The *S.code* can be calculated as follows:

$$S.code = \frac{x_2 - x_0}{x_2 - x_1} \times 2^n \tag{9}$$

## III. Space-Value-Based Code Value Correction

We established a novel code position correction method based on spatial position to ensure the correct connection between *R.code* and *S.code*. A schematic diagram of the grating we used is shown in Fig. 2. The $N$-bit *R.code* was calculated by the decoding method described in Section II-A; the angular displacement subdivision algorithm proposed in Section II-B was used to obtain the $n$-bit *S.code*. We then connected *R.code* with *S.code* as discussed below.

The edge contour of the raster line image is blurred due to the circular grating scoring and light diffraction phenomenon. When *S.code* needs to carry or borrow as the grating is rotated, *R.code* changes in advance or delays thus generating an error code.

When the grating reference reticle is coded by Gray code, as shown in Fig. 4, decoding is performed at $x = x_l$ and $x = x_r$ on both sides of the image detector center line. According to the range of *S.code*, determine and choose the current *R.code*. At $x = x_l$, $\alpha_l$ is "1110111"; at $x = x_r$, $\alpha_r$ is "1110101", $x_l$ and $x_r$ satisfy the following:

$$|x_l - x_r| < \frac{1}{2} \times T \tag{10}$$

where $T$ is the number of pixels between the centroids of two adjacent subdivision reticles. As shown in Fig. 4, under certain circumstances, an error code may generated when $\alpha_l \neq \alpha_r$. The current *R.code* is determined by setting the threshold $Y_c$ and comparing it with *S.code*.

$$Y_c = \frac{|x_l - x_r|}{T} \times 2^n \tag{11}$$

- When $S.code < Y_c$, *R.code* selects the code value at $x = x_l$ (Fig. 4), $\alpha_l$ = "1110111", after the Gray code is decoded, *R.code* = "1011010";

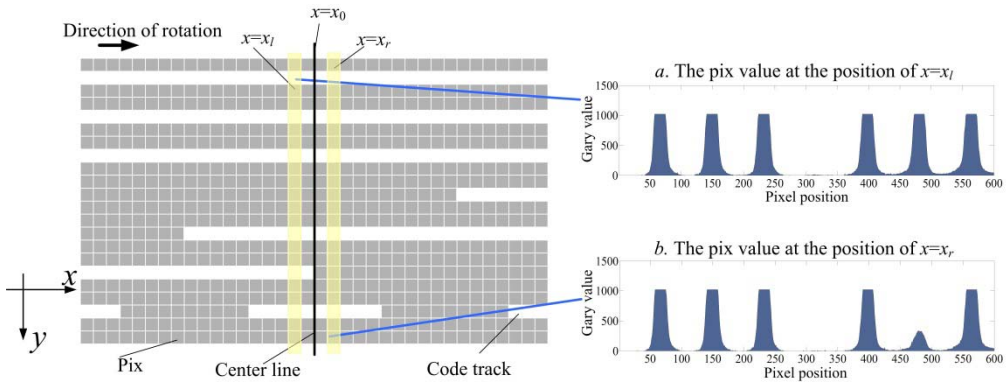


Fig. 4. Code value space position correction.

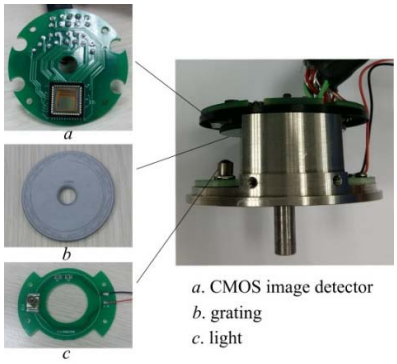


Fig. 5. Experimental device (physical diagram).

- When $S.code \geq Y_c$, $R.code$ selects the code value at $x = x_r$ (Fig. 4), $\alpha_r =$ "1110101", after the Gray code is decoded, $R.code =$ "1011001".

Through the above correction, when the $S.code$ needs to carry or borrow, the $R.code$ changes in time to connect the code values as the grating is rotated.

## IV. Experiment

We conducted an experiment to verify the proposed angular displacement measurement mechanism. We designed the measuring device shown in Fig. 5 which consists of a flange, a parallel light source, a grating, an image detector, and a data processing circuit. The device has a diameter of 40 mm and a height of 35 mm with shell.

During operation, the image detector sends the collected grating pattern information to the control chip for sorting and calculation, then uploads it to the host computer for display and monitoring through Cameralink. The hardware parameters of the designed image angular displacement measurement system are shown in Table 1.

The grating was made by attaching etched metal chromium to the glass substrate, as shown in Fig. 5(b). The grating diameter is 38 mm. Gray code was used to score seven circle reference reticles (i.e. $2^7$ $R.codes$) of 0.1 mm width each; the interval between adjacent reticles is 0.3 mm. The outer ring is composed of 0.7 mm × 0.2 mm subdivided reticles uniformly distributed in the radial direction at equal intervals for sub-pixel level angular displacement subdivision.

TABLE I

Image Type Angular Displacement Measurement System Hardware Parameters

| | |
|---|---|
| Light source | |
| Wavelength | λ=460 nm |
| Type | LED |
| CMOS image detector | |
| Model | NOIV1SN1300A |
| SXGA | 1280×1024 active pixels |
| Pixel size | 4.8 um×4.8 um |

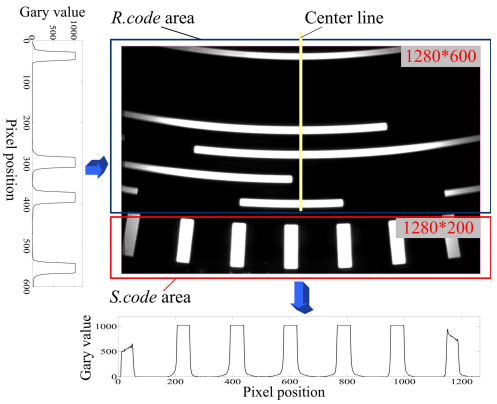


Fig. 6. Image detector configuration.

### A. Image Detection Experiment

The image detector configuration is shown in Fig. 6. We set the image recognition area of the detector to 1280 × 800, wherein the $R.code$ identification area is 1280 × 600 and the $S.code$ identification area is 1280 × 200. We identified the $R.code$ value at the center line of the image detector, scanned to identify the subdivision reticle, and performed subdivision calculation to determine $S.code$.

The image angular displacement measuring device was driven by a light source with wavelength of 460 nm to minimize the effects of diffraction on the imaging of circular gratings. Transmissive illumination makes the grayscale value of the grating image of the reticle portion large while that of the chrome-plated portion is small. To eliminate the influence of uneven illumination and factors (Fig. 6), we performed an

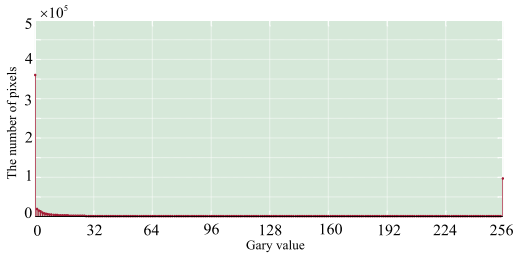


Fig. 7. Grayscale histogram of raster disk image.

image quality analysis by intercepting 800 ∗ 800 near the center line as shown in Fig. 7.

Figure 7 shows the gray histogram of the raster code disk image. The contrast of the grating image is relatively large. The distribution of pixel values in the light transmissive area and the non-transmissive area is relatively concentrated, and the reticle of the grating is easy to distinguish. The number of pixels in the background is 359,950 and the number of pixels in the reticle is 96,950. We sought to exclude background and reticle pixels as the number of noise pixels is 183,100. The signal to noise ratio of the sub image is:

$$SNR = \frac{359950 + 96950}{183100} \times 100\% = 249.5\% \qquad (12)$$

The circular raster image quality is good as per the results of Eq. (12).

### B. Resolution Verification

The reference reticle of the grating was coded in Gray code. To verify the resolution of the proposed device, we determined the $N$-bit Gray code value $\alpha$ as discussed in Section II-A and decoded it into an $N$-bit binary reference code *R.code* by Eq. (13):

$$\begin{cases} R.code\,(i) = \alpha\,(i) & i = N \\ R.code\,(i) = \alpha\,(i+1) \oplus \alpha\,(i) & i = 0, 1, \ldots, N-1 \end{cases} \qquad (13)$$

where $R.code(i)$ represents the natural binary reference code of the $i$-th bit, $\alpha(i)$ represents the Gray code value of the $i$-th bit, and "⊕" represents the "XOR" operation.

We next applied the sub-pixel angular displacement subdivision algorithm (Section II-B) to calculate the $n$-bit *S.code*, rotated the main axis of the measuring device, and observed the binary value of the output angle. We found that the device can realize 14-bit angular displacement subdivision ($n = 14$) and achieved a total of 21-bit angular displacement measurements. A conventional angular displacement measuring device of the same size achieves an 18-bit angular displacement measurement at most; compared to the conventional measuring device, the resolution of the proposed device is markedly higher.

The code value correction (Section III) ensures that $x_l = 634$ and $x_r = 646$, *R.code* and *S.code* are connected. As per the grating scribing, $T \approx 180$ and $|x_l\text{-}x_r| = 12$ satisfies Formula (5). We rotated the grating over the course of a circular and no error code was produced. Figure 8 shows a schematic diagram of the device's angle information.

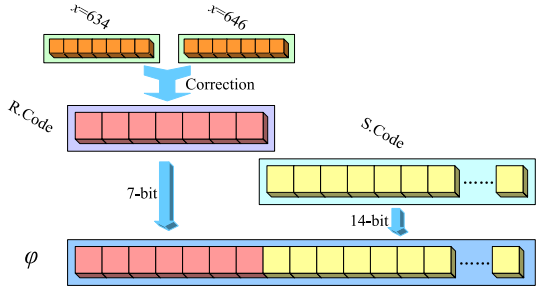


Fig. 8. Angle information (schematic diagram).

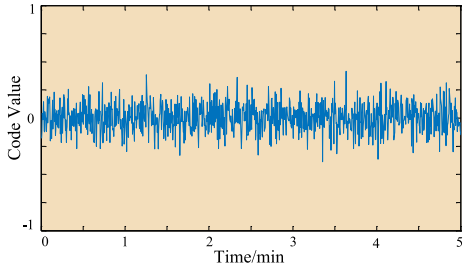


Fig. 9. Resolution stability test.

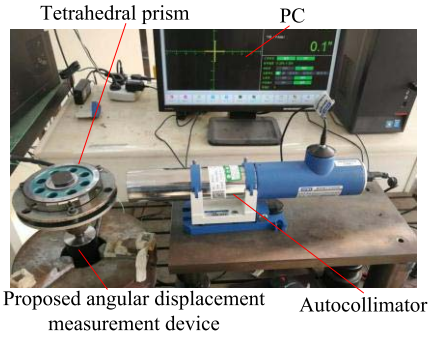


Fig. 10. Schematic diagram of experimental setup.

As shown in Fig. 8, the absolute angular position can be expressed as follows:

$$\varphi = R.code \times 2^{14} + S.code\ \ (21 - bit) \qquad (14)$$

We next determined the stability of the *S.code* to verify the resolution of the device. As shown in Fig. 8, the stability of the LSB of *S.code* determines the resolution of the measuring device. We observed the changes in the LSB value of *S.code* to draw the variation curve shown in Fig. 9. The value of this bit is stable, which suggests that 21-bit angular displacement measurement can be accurately realized via the proposed device.

### C. Accuracy Verification

In order to verify the accuracy of the proposed angular displacement measuring device, we used a 24-degree prism and laser autocollimator to detect the error as shown in Fig. 10. The 24-face prism was connected to the device via coupling and the difference between the displayed values of the two was recorded as the measurement error.

When performing the accuracy test, the detection was started from an absolute angular position of 0°. Errors were

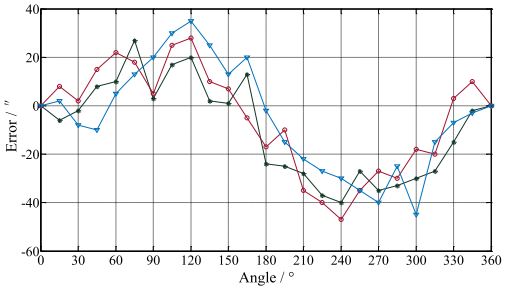


Fig. 11. Error curve.

TABLE II
DETECTION RESULTS

| Angles | Average | Angles | Average |
|---|---|---|---|
| 0° | 0″ | 195° | -16.67″ |
| 15° | 1.33″ | 210° | -28.33″ |
| 30° | -2.67″ | 225° | -34.67″ |
| 45° | 4.33″ | 240° | -39″ |
| 60° | 12.33″ | 255° | -32.33″ |
| 75° | 19.33″ | 270° | -34″ |
| 90° | 9.33″ | 285° | -29.33″ |
| 105° | 24″ | 300° | -31″ |
| 120° | 27.67″ | 315° | -20.67″ |
| 135° | 12.33″ | 330° | -6.33″ |
| 150° | 7″ | 345° | 1.67″ |
| 165° | 9.33″ | 360° | 0″ |
| 180° | -14.33″ | | |

recorded every 15° according to the working principle of polyhedron detection. The error recording was performed in three independent replications to verify the repeatability of the measurement device and reduce random errors. The accuracy detection results are shown in Fig. 11.

The mean value of the three independent experiments was used as the angle error detection result of the image type angular displacement measuring device, as shown in Table 2. The mean square error of the error mean in Table 2 was calculated by the standard deviation formula. The accuracy of the proposed angular displacement measuring device is 20.14".

## V. CONCLUSION

We developed an image-based technique in this study to realize small-scale, high-resolution, and high-precision angular displacement measurement. We first established the image angular displacement measurement mechanism, circular grating decoding method, and sub-pixel subdivision algorithm. We then built a code value correction algorithm to solve the error code problem when the subdivision code and the reference code are connected. Finally, we ran a series of experiments to validate the proposed theory.

The image angular displacement measuring device described in this paper may provide a workable foundation for further research on fine photoelectric measuring instruments.We also hope to have delineated a new direction for studying high-precision high-resolution angular displacement measuring technology.

## REFERENCES

[1] L. Qiang, L. Wen-Hao, Bayinhexige, B. Yang, L. Zhao-Wu, and W. Wei, "Interferometric precision displacement measurement system based on diffraction grating," *Chin. Opt.*, vol. 10, no. 1, pp. 39–50, 2017.
[2] H. B. Zhang, Q. H. Wan, S. J. Wang, H. Yu, and L. H. Liang, "Installation error control of dynamic measurement for small photoelectric encoder," *Chin. Opt. Precis. Eng.*, vol. 24, no. 7, pp. 1655–1660, 2016.
[3] O. U. Lashmanova, A. S. Vasileva, A. V. Vasileva, A. G. Anisimov, and V. V. Korotaev, "High-precision absolute linear encoder based on a standard calibrated scale," *Measurement*, vol. 123, pp. 226–234, Jul. 2018.
[4] G. Ye, H. Liu, Y. Ban, Y. Shi, L. Yin, and B. Lu, "Development of a reflective optical encoder with submicron accuracy," *Opt. Commun.*, vol. 411, pp. 126–132, Mar. 2018.
[5] J. Deng *et al.*, "Eightfold optical encoder with high-density Grating," *Appl. Opt.*, vol. 57, no. 10, pp. 2366–2375, 2018.
[6] M.-S. Wei, F. Xing, and Z. You, "A real-time detection and positioning method for small and weak targets using a 1D morphology-based approach in 2D images," *Light, Sci. Appl.*, vol. 7, p. 18006, May 2018.
[7] R. Zhao *et al.*, "Multichannel vectorial holographic display and encryption," *Light, Sci. Appl.*, vol. 7, Nov. 2018, Art. no. 95.
[8] W. Luo, Y. Zhang, A. Feizi, Z. Göröcs, and A. Ozcan, "Pixel super-resolution using wavelength scanning," *Light, Sci. Appl.*, vol. 5, Apr. 2016, Art. no. e16060.
[9] V. Bianco *et al.*, "Strategies for reducing speckle noise in digital holography," *Light, Sci. Appl.*, vol. 7, Aug. 2018, Art. no. 48.
[10] F. Merola *et al.*, "Tomographic flow cytometry by digital holography," *Light, Sci. Appl.*, vol. 6, Apr. 2017, Art. no. e16241.
[11] D. B. Leviton and B. Frey, "Ultra-high resolution, absolute position sensors for cryostatic applications," *Proc. SPIE*, vol. 4850, pp. 776–787, Mar. 2003.
[12] D. B. Leviton "New ultra-high sensitivity, absolute, linear, and rotary encoders," in *Proc. SPIE, Photon. Space Environ.*, San Diego, CA, USA, vol. 3440, Jul. 1998, pp. 100–111.
[13] H. Yu *et al.*, "Error-correct arithmetic for angular displacement measurement with single linear image detector," *Opt. Eng.*, vol. 57, no. 5, 2018, Art. no. 054108.
[14] J. S. Bajić, D. Z. Stupar, B. M. Dakić, M. B. Živanov, and L. F. Nagy, "An absolute rotary position sensor based on cylindrical coordinate color space transformation," *Sens. Actuators A, Phys.*, vol. 213, pp. 27–34, Jul. 2014.
[15] Y. Sugiyama *et al.*, "A 3.2 kHz, 14-bit optical absolute rotary encoder with a CMOS profile sensor," *IEEE Sensors J.*, vol. 8, no. 8, pp. 1430–1436, Aug. 2008.
[16] H. Kim, Y. Yamakawa, T. Senoo, and M. Ishikawa, "Visual encoder: Robust and precise measurement method of rotation angle via high-speed RGB vision," *Opt. Express*, vol. 24, no. 12, pp. 13375–13386, 2016.
[17] M. Tresanchez, T. Pallejà, M. Teixidó, and J. Palacín, "The optical mouse sensor as an incremental rotary encoder," *Sens. Actuators A, Phys.*, vol. 155, no. 1, pp. 73–81, 2009.
[18] M. Tresanchez, T. Pallejà, M. Teixidó, and J. Palacín, "Using the image acquisition capabilities of the optical mouse sensor to build an absolute rotary encoder," *Sens. Actuators A, Phys.*, vol. 157, pp. 161–167, Jan. 2010.
[19] J.-A. Kim, J. W. Kim, C.-S. Kang, J. Jin, and T. B. Eom, "Absolute angle measurement using a phase-encoded binary graduated disk," *Measurement*, vol. 80, pp. 288–293, Feb. 2016.
[20] H. Yu, Q. Wan, X. Lu, Y. Du, and S. Yang, "Small-size, high-resolution angular displacement measurement technology based on an imaging detector," *Appl. Opt.*, vol. 56, no. 3, pp. 755–760, 2017.
[21] A. Lutenberg, F. Perez-Quintián, and M. A. Rebollo, "Optical encoder based on a nondiffractive beam," *Appl. Opt.*, vol. 47, no. 13, pp. 2201–2206, 2008.